Verdon, J. P., Horne, S. A., Clarke, A., Stork, A. L., Baird, A. F., & Kendall, J-M. (2020). Microseismic monitoring using a fibre-optic Distributed Acoustic Sensor (DAS) array. *Geophysics*, 1-96. https://doi.org/10.1190/geo2019-0752.1

Microseismic monitoring using a fibre-optic Distributed Acoustic Sensor (DAS) array

James P. Verdon[1] *, Steve A. Horne[2], Andrew Clarke[3], Anna L. Stork[1,3], Alan F. Baird[1], J-Michael Kendall[1]

1. School of Earth Sciences, University of Bristol, Wills Memorial Building, Queen's Road, Bristol, U.K., BS8 1RJ.

2. Formerly at Chevron Energy Technology Company, 1 Westferry Circus, Canary Wharf, London, U.K., E14 4HA. Now at Lytt, Hopton Street, London, U.K., SE1 9LQ.

3. Silixa Ltd., 230 Centennial Ave, Elstree, Borehamwood, U.K., WD6 3SN.

* Corresponding Author. Email: James.Verdon@bristol.ac.uk, Tel: 0044 117 331 5135.

Right running head: Microseismic monitoring using a DAS array

Acknowledgements

The authors would like to thank Chevron USA for providing the dataset, and allowing us to publish. This work was funded by the Natural Environment Research Council (NERC) under the FAST-MoDE project (Grant No. NE/R014531/1).

ABSTRACT

We present a case study demonstrating the use of an "L"-shaped downhole fibre-optic array to monitor microseismicity. We use a relatively simple method to detect events from continuous waveform data, and develop a workflow for manual event location. Locations are defined with a cylindrical coordinate system, with the horizontal axis of the DAS cable being the axis of symmetry. Events are located using three manual "picks", constraining (1) the zero-offset "broadside" channel to the event (2) the P-S wave arrival time difference at the broadside channel, and (3) the angle, θ of the event from the array. Because the one-component DAS array is unable to record P-wave energy on the broadside channel, the P-wave pick is made indirectly by ensuring that the modeled P- and S-wave moveout curves match the observed data. The θ angle requires that signal is observed on the vertical part of the array, in our case this is possible because an engineered fiber, rather than standard telecommunications fiber, provided a significant reduction in the noise level. Because only three picks need to be made, our manual approach is significantly more efficient than equivalent manual processing of downhole geophone data, where picks for P- and S-waves must be made for each receiver. We find that the located events define a tight cluster around the injection interval, indicating that this approach provides relatively precise and accurate event locations. A surface microseismic array was also used at this site, which detected significantly fewer events, the locations of which had significantly greater scatter than the DAS array locations. We conclude by examining some other aspects of the DAS microseismic data, including the presence of multiple events within very short time windows, and the presence of converted phases that appear to represent scattering of energy from the hydraulic fractures themselves.

INTRODUCTION

The use of fiber-optic cables as Distributed Acoustic Sensing (DAS) arrays for recording downhole seismic data is becoming increasingly common. The predominant application thus far has been for Vertical Seismic Profiling (e.g., Parker et al., 2014; Mateeva et al., 2014; Daley et al., 2016). However, the use of DAS for microseismic monitoring during hydraulic fracturing has also shown significant potential (e.g., Webster et al., 2016; Molteni et al., 2017; Karrenbach et al., 2017, 2019; Mondanos and Coleman, 2019).

DAS arrays provide a number of advantages over downhole geophones. The fiber-optic cable can be placed behind the casing of a well, such that a well can be used both to monitor, and to inject or produce fluid, with minimal intervention. While geophones can be placed behind casing, this is rarely done in practice. Moreover, DAS array "channels" (individual recording points) can be closely spaced along the fiber (typically spacing is at the scale of meters), so a single cable installed along a well provides very high data fold. Downhole geophone arrays for microseismic monitoring typically use 10 – 50 geophones (e.g., Maxwell et al., 2010), whereas a DAS array provides 1000s of channels. Surface-based microseismic monitoring (e.g., Chambers et al., 2010) typically uses thousands of stations – however, in such settings the stations are separated from the reservoir by thousands of meters of overburden rock, which effects the ability of the array to both detect and locate microseismic events.

However, DAS arrays also pose several challenges for effective microseismic monitoring. DAS arrays provide a single component (1C) of measurement, providing axial strain along the cable, while geophone arrays provide three-component (3C) data, such that the particle motion of the arriving seismic waves can be observed and used to aid in the event location process (e.g., Jones et al., 2010). The single-component nature of DAS array data creates additional challenges because it cannot record waves traveling perpendicular to the array (so-called broadside arrivals). This is because P-waves travelling perpendicular to the array have no strain component oriented along the cable, and while broadside S waves can, depending on their polarisation, have a component of particle motion along the axis of the cable, the strain rate imparted is also zero, and so no signal is recorded (Baird et al., 2019).

The high data fold described above as an advantage also presents a challenge for DAS arrays. Microseismic data are most effective when used in real time to guide operational decisions (e.g., Clarke et al., 2019). Therefore, large amounts of data must be handled quickly to provide real-time microseismic monitoring using a DAS array.

In this paper we present a case study of microseismic acquired with a DAS array. We use a simple but effective procedure to detect events, and develop a processing workflow to manually pick and locate events. In this case example an engineered fiber-optic cable was used, which increases the Rayleigh light back-scatter, resulting in improved sensitivity, and thus more signal observed across the array. This allowed signals to be recorded on both the horizontal and vertical parts of an “L”-shaped array, and thereby resolving the angular ambiguity that is otherwise present for a single-component, linear-shaped array. A surface-based geophone array was also used to acquire microseismic data at this site, allowing us to compare the performance of the DAS array to other types of microseismic data. We also highlight some interesting aspects of microseismic waveforms that can be observed with the high-fold downhole acquisition provided by a DAS array.

Case Study Description

In this paper we present results from a DAS array used to monitor hydraulic fracturing. Figure 1 shows the monitoring setup. Multiple horizontal wells were drilled from a single pad, and a fiber-optic cable was installed behind casing in one of the wells. We have continuous monitoring data over a period of 200 minutes as a single stage of hydraulic fracturing was conducted in an adjacent well, sampled at 2000 Hz. To give an idea of the data volumes generated by DAS arrays, this 200 minute period covering a single fracturing stage comprises 40 GB of raw data (stored as 16-bit integer Numpy “.npz” arrays, a compressed binary format containing only the data array and no metadata).

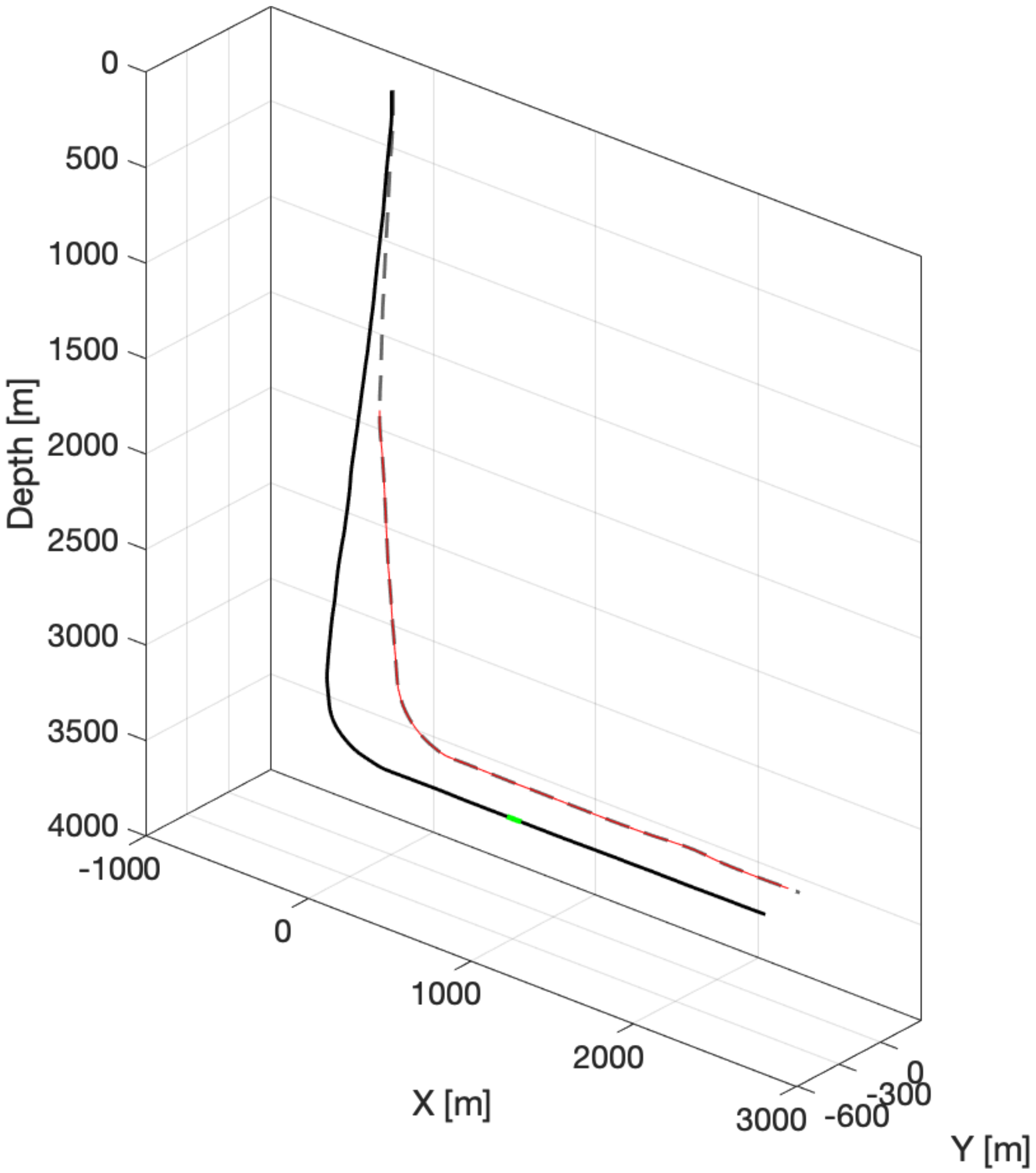

Figure 1: Monitoring setup for our case study. Two horizontal wells are drilled from the same pad to a depth of 3370 m. The dashed grey line shows the monitoring well in which the fiber-optic cable was deployed – the active channels of the DAS array are marked by the red line. The solid black line shows the hydraulic fracturing well. Fracturing stages were conducted along the well – here we present data from a single stage, marked in green. We define the x- and y- axes as running parallel and perpendicular to the well trajectories.

DAS arrays make use of Rayleigh scattering of light along a fiber-optic cable. An interrogator unit emits a pulse of laser light into the cable and computes the strain rate along the cable from phase changes within the backscattered energy. Initial DAS deployments commonly used conventional fiber-optic cable, which is designed primarily to transmit telecommunication signals, and therefore to minimize scattering. However, the latest generation of DAS arrays use fiber-optic cables designed specifically for the purpose, and therefore scatter a larger proportion of the light pulse. This produces a significant improvement in the signal quality (Richter et al., 2019). This case study uses a Silixa Carina® Sensing System engineered cable and interrogator. A direct comparison between cable types is not possible in this case as no conventional cable was deployed alongside the engineered fiber. However, the engineered cable and interrogator system were able to detect clear signals for most of our detected events along both the horizontal and vertical parts of the cable, even for events that are a substantial distance (approximately 1 km) from the vertical part of the well. This has often not been the case for previous DAS microseismic cases, where signals have typically been detected only in the horizontal part of the cable, unless events were particularly large, or close to the vertical part of the array (e.g., Webster et al., 2016; Karrenbach et al., 2017; 2019). Unless, signals are recorded on both vertical and horizontal parts of the array, the event position cannot be fully constrained. We note that, as DAS interrogator technology continues to develop, it may be the case that the technology improves to the point that the noise level, even with standard telecommunications fiber, falls below the lower seismic noise floor, at which point the choice of fibre will become immaterial.

The total fiber-optic cable length in the monitoring well was 5,673 m, although data were recorded from the lower 3958 m only. The gauge length for each channel in 10 m, with each “channel” being spaced at 2.028 m, giving 1952 total channels. Data from the first 60 and last 37 channels were very noisy, and were removed from our analysis, leaving 1855 channels. The first 650 channels were in the vertical section of the well, channels 650 to 900 were in the build (i.e. curved) section of the well, and channels 900 and greater were in the horizontal section, giving the overall DAS array an “L” shape (Figures 1 and 2). We use a 1D block velocity model, derived from a sonic log acquired in a nearby vertical well (Figure 3), where the velocity of each block, spaced at 10 m intervals, is taken as the mean of the sonic log within this interval.

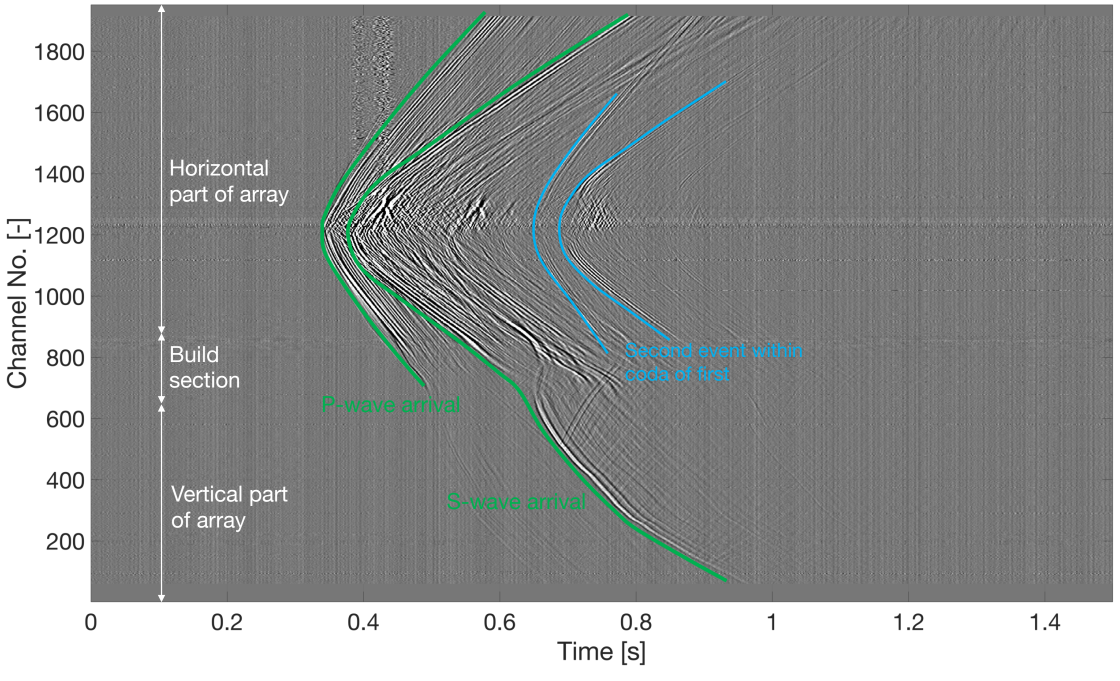

(a)

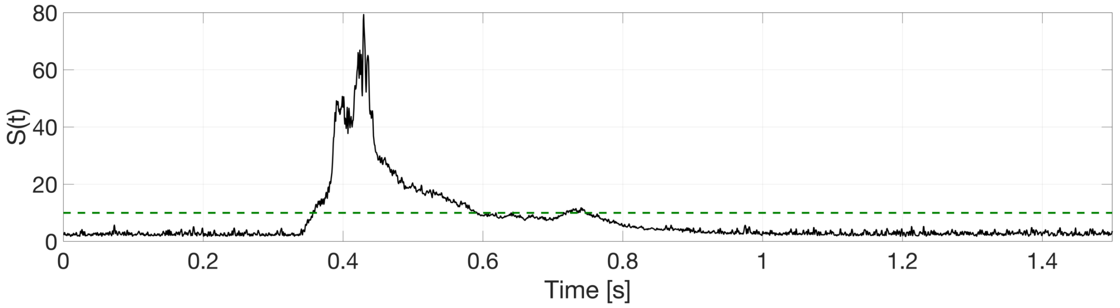

(b)

Figure 2: Example microseismic event recorded by the DAS array. The moveout of the P- and S-wave arrivals can be observed on both the horizontal and vertical parts of the array. A second event is also visible within the coda of the first. In (b) we show the stack of absolute values over all traces (S(t)). The background noise falls below our detection threshold of ten (green dashed line), while the microseismic events exceed it.

Surface-based microseismic data were also acquired at this site, using a large number of surface geophones and a beamforming approach (e.g., Chambers et al., 2010). In total, 49 events were recorded by the surface array during the period studied here. The event catalogue generated from the surface array was provided to us, however the original waveforms were not available. Therefore, we are reliant on the catalogue as provided to the operator by a processing contractor, and we are not able to make an independent quality assessment of the surface microseismic data. Evidently, this does not make for an ideal comparison, since we are not able to rule out the surface array detection performance or location accuracy being affected by the selection of processing method, such as by a poor choice of velocity model, for example. Nevertheless, microseismic acquisition of this type using a large surface array with events detected via a beamforming algorithm represents a relatively standard practice for the industry (e.g., Chambers et al., 2010; Duncan and Eisner, 2010), and the dataset represents an example of the typical data quality produced by commercial providers, and so makes for a relevant comparison with the DAS array.

Similarly, while the surface array provides a useful means of comparing the typical quality of data provided by different types of monitoring arrays, we are not able to directly compare the recorded waveforms, nor can we attempt a joint analysis of the microseismicity using both arrays.

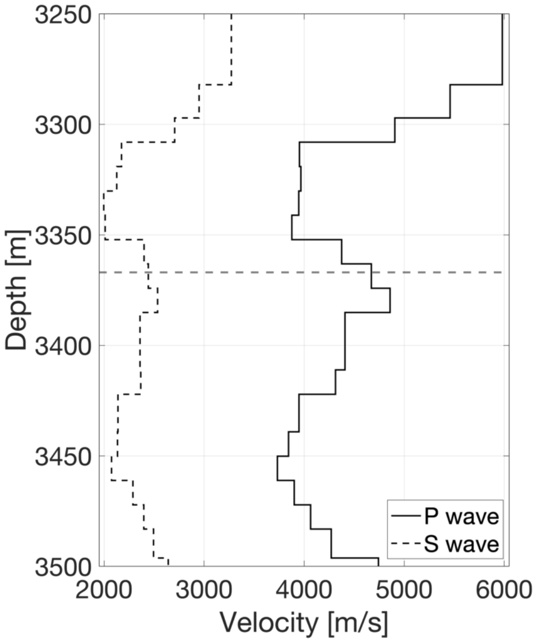

Figure 3: The 1D block velocity model for P and S waves. The dashed grey line at 3367 m marks the mean depth of the horizontal portion of the monitoring well.

DETECTING AND LOCATING MICROSEISMIC EVENTS USING DAS

Event Detection

When downhole geophones are used for microseismic monitoring, event detection methods are similar to those used to detect earthquakes with global seismometer networks. Identification of spikes in running short-term average/long-term average ratios (STA/LTA) is probably the most often-used approach for event detection (e.g., Allen, 1978): if STA/LTA values exceed a specified threshold simultaneously on a sufficient number of stations, a potential event is declared (e.g., Lomax et al., 2012). Alternatively, other statistical measures such as the Akaike Information Criteria (e.g., Sleeman and van Eck, 1999), signal polarity (e.g., Kurzon et al., 2014), or kurtosis (e.g., Tselentis et al., 2012) are commonly used.

These methods require a running computation of statistical parameters on a trace-by-trace basis. This will be computationally expensive for real-time analysis of DAS array data consisting of thousands of channels. Current research is focussed on using machine learning to identify microseismic events in DAS data, treating the raw data as a 2D image in space and time and using image-recognition software to detect events (e.g., Binder and Chakraborty, 2019).

Here we use a more “rough-and-ready” approach to event detection. Figure 2 shows an example event, and Figure 2b shows the sum of the absolute values of the recorded data over all channels:

$$S(t) = \frac{\sum_{i=1}^{n} |s_i(t)|}{n},$$

where n is the number of channels, and $s_i(t)$ is the signal recorded on channel i at time t. We apply a low-pass filter at 300 Hz to supress high-frequency noise as the sole pre-processing step prior to this operation. Although the recorded arrivals move out across the array with time, the array has sufficient spatial sampling such that a clear pulse is seen on the stacked trace where a signal is present, whereas noise on individual traces is supressed by the averaging procedure represented by the stacking. We use this as the basis of our event detection, selecting candidate events when the stack exceeds a selected threshold, in this case a value of $S(t) > 10$, based on typical stack values when no signal is present (Figure 2b).

Where the stack exceeds this threshold we declare a potential event, saving the preceding 0.25 s of data, and the following 1.0 s of data, for further analysis. This approach produced 384 triggers. Manual analysis of these triggers showed that 42 were coherent noise spikes (see Figure 4). The cause of these spikes has not as yet been determined, and we do not consider them further here.

The remaining 342 triggers were all microseismic events, a rate of event occurrence of an event approximately every 35 s. Therefore, all of the triggers identified by this simple detection method were from coherent “events” (either a microseismic event or a noise spike event); none were produced by the random background noise. Of these, 90% were microseismic events and 10% were noise spikes. Despite the simplistic nature of our detection mechanism, this was sufficient for manual processing purposes, finding a substantial number of events detected with a minimal number of false positives. DAS arrays produce large volumes of data, which would be computationally expensive to process if done in the same way as geophone data. However, here we show that simple alternatives can provide effective performance, taking advantage of the high data fold to supress background noise and identify coherent signals. That said, we re-iterate the fact that the current state-of-the-art methods include the use of machine-learning-based image recognition software to identify events, treating the data plotted in space and time (e.g., Figure 2) as a 2D image (e.g., Binder and Chakraborty, 2019); the use of migration-based methods to focus observed arrivals at source locations; and the use of full waveform inversion.

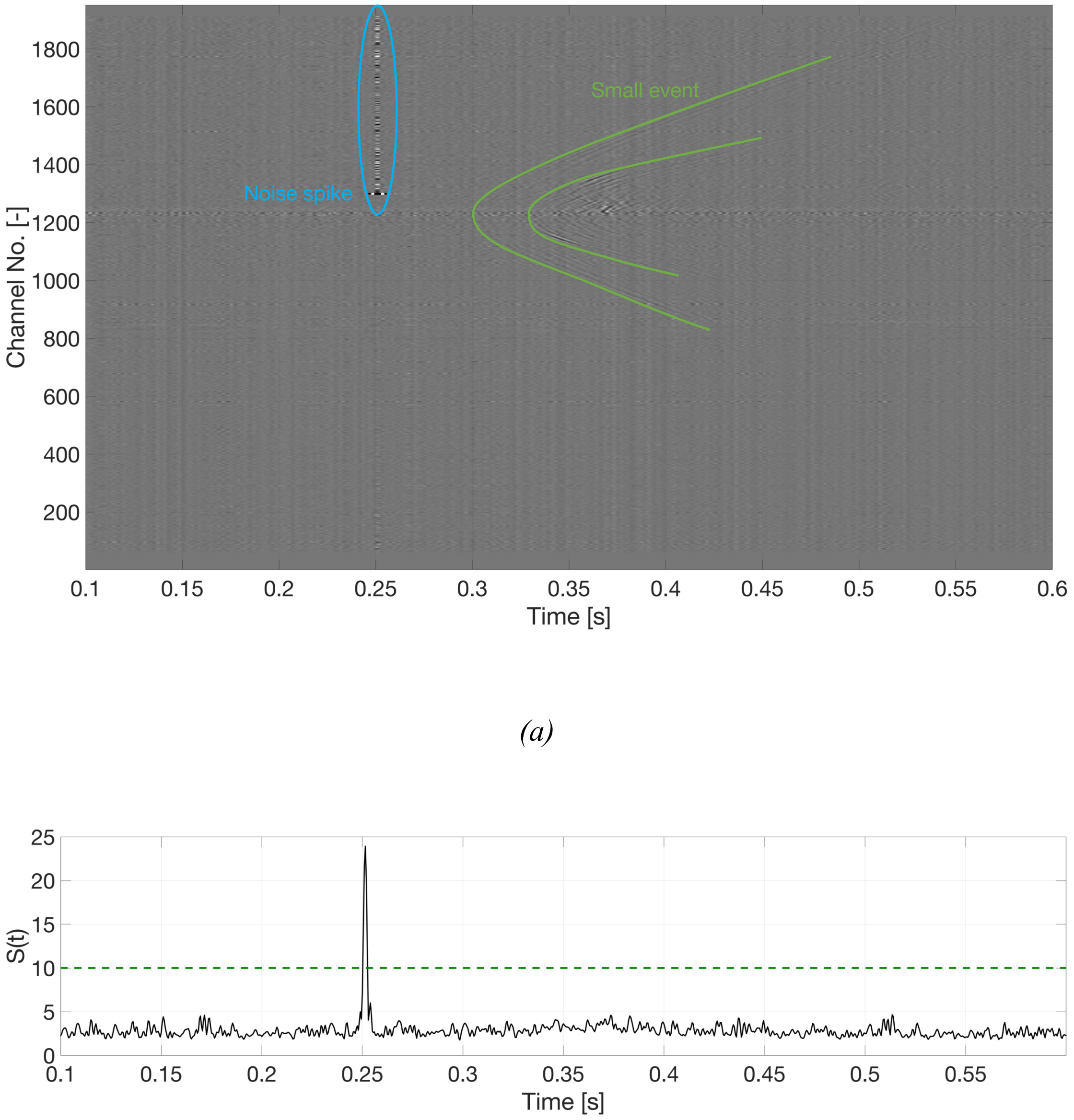

(a)

(b)

Figure 4: Noise spike identified by out detection algorithm. A spike is seen on channel 1290, extending to the end of the cable with zero moveout. A small event is also visible, although it is not large enough to be picked up by the detection method.

Manual Event Location

The simplest and most commonly-used method for locating microseismic events recorded with downhole geophones is to make picks, either manually or using an auto-picker (e.g., Lomax et al., 2012) of the P- and S-wave arrival times at each receiver, and invert these for the best-fitting event location that minimizes the residuals between observed and modelled travel times. Note that throughout this paper, we use an Eikonal solver (Sethian and Popovici, 1999) to model travel times through the 1D velocity model shown in Figure 3.

With over 1,900 individual channels, however, it is clear that manual picking of this kind as done by, for example, Karrenbach et al. (2019) may be impractical for rapid analysis of DAS microseismic data. Guided or semi-automatic interactive picking could have a role to play here. Picks could be made automatically on a trace-by-trace basis, but this will again be computationally expensive to do, and with 1C data it may be difficult to determine whether automated picks represent P- or S-wave arrivals, whereas the orthogonal polarity of these phases can be used as a discriminator when 3C data are available (e.g., Oye and Roth, 2003).

Instead, we develop a manual processing workflow that takes advantage of the fact that, for DAS array data, events can be located using a cylindrical coordinate system with the longitudinal axes running along the horizontal portion of the fiber (Figure 5).

The first coordinate is the nearest channel to the event, r_c, which can be identified as the channel at the apex of the hyperbolic P- and S-wave moveout curves. We also refer to this as the broadside, or zero-offset, channel, as this is the point at which the arrivals are travelling at 90° to the cable axis.

The distance of the event from the array, $d_{S\text{-}P}$, is defined by the difference in arrival times between the P- and S-waves at the zero-offset channel. This distance will also affect the shape of the P- and S-wave moveout hyperbolae across all channels. These parameters, r_c and $d_{S\text{-}P}$, define a circular event locus around the cable – the position of the event around this circle is constrained by the polar angle θ within the polar coordinate system defined in Figure 5, defined in this case as the angle clockwise from the vertical.

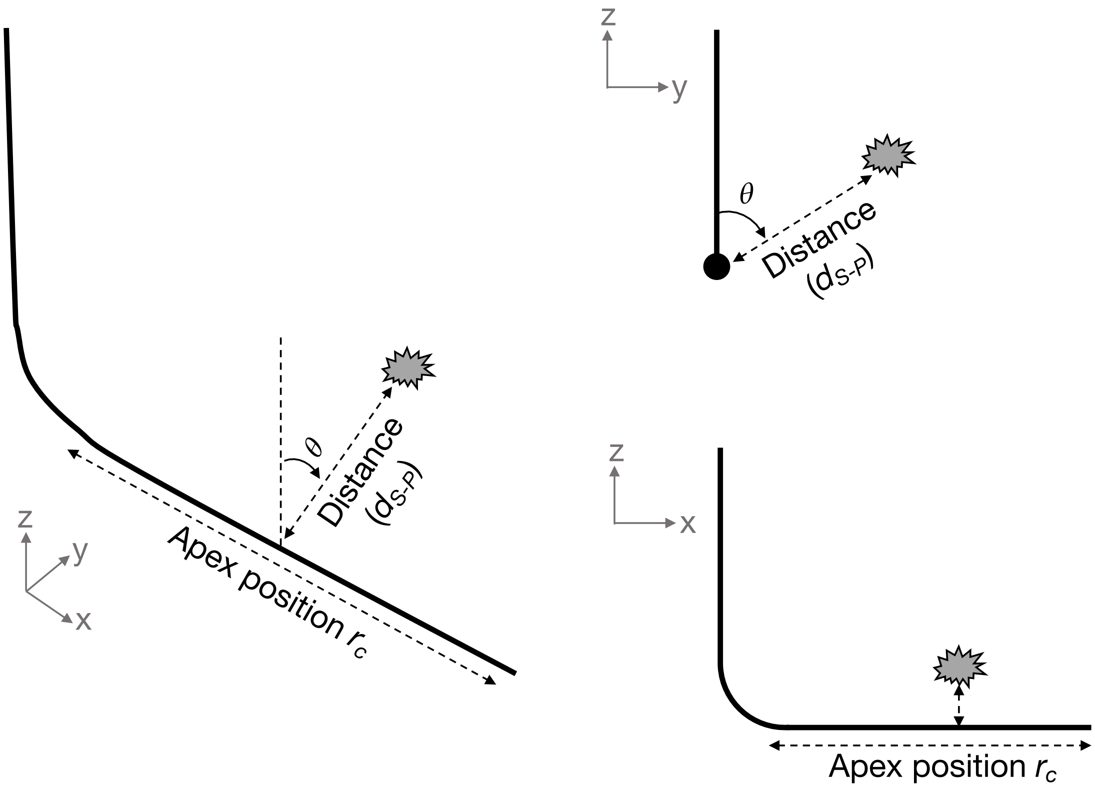

(a)

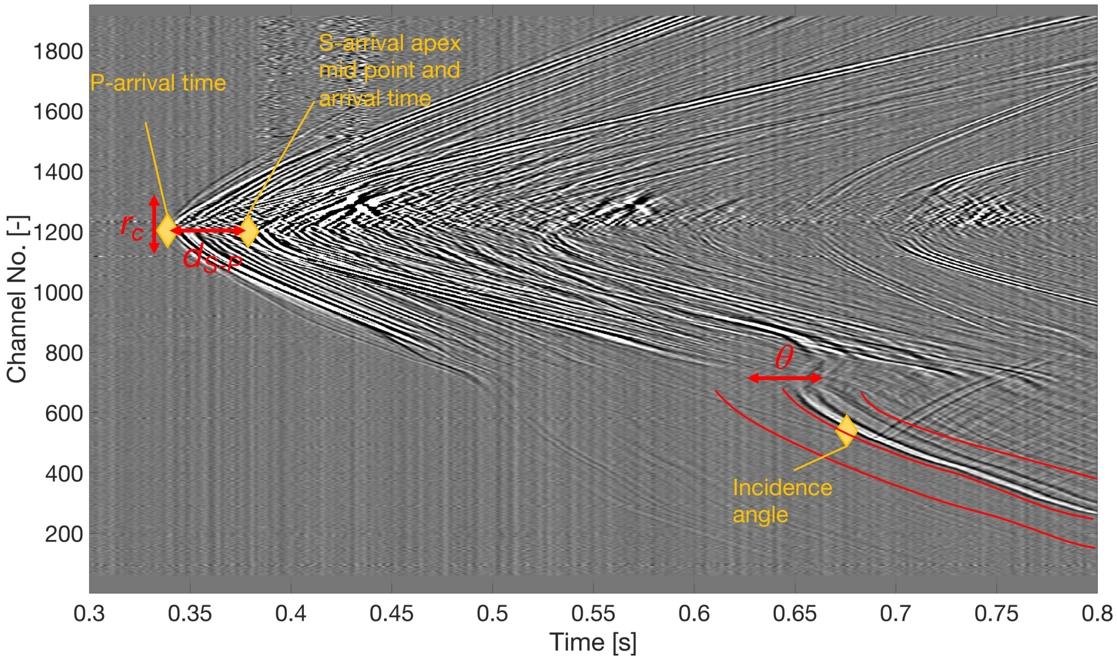

(b)

Figure 5: Schematic representation of our event location procedure. In (a) the event location (grey symbol) is defined by three coordinates (representing a cylindrical coordinate system with longitudinal axis along the horizontal portion of the well), shown as a 3D projection (left), and along (upper right) and perpendicular to (lower right) the fiber axis. The position of the nearest (i.e. broadside) channel along the cable, r_c, the distance of the event from the cable, which is determined from the differential arrival times between P and S waves, d_{S-P}, and the angle θ. In (b) we show the three picks that are necessary to define these coordinates: the mid-point of the S wave hyperbola, the times of the first P and S wave arrivals, and the position of the arrivals on the vertical part of the array, which are primarily determined by the θ angle.

We consider some practicalities of locating events in this way below. Firstly, we note that only three "picks" need to be made to locate an event: the apexes of the P- and S-wave arrival hyperbolae, and the θ angle of the event from well (Figure 5). Therefore, despite the substantially larger volumes of data involved, manual processing of DAS microseismic data actually becomes faster than manual picking of geophone data, where P- and S-wave picks must be made for each station (so, for example, with a 12-geophone array, 24 individual picks must be made).

Figure 6 shows a close-up view of the P- and S-wave hyperbolae apexes. We note a loss of P-wave energy at apex position. This is because the P waves are arriving broadside to the cable, and so there is no component of motion along the cable to be recorded. This presents a challenge with respect to picking both the time and the broadside channel for the P-wave apex. In contrast, at the S-wave apex we observe a polarity flip in the S wave, caused because the DAS array records strain-rate along the cable, rather than particle velocity.

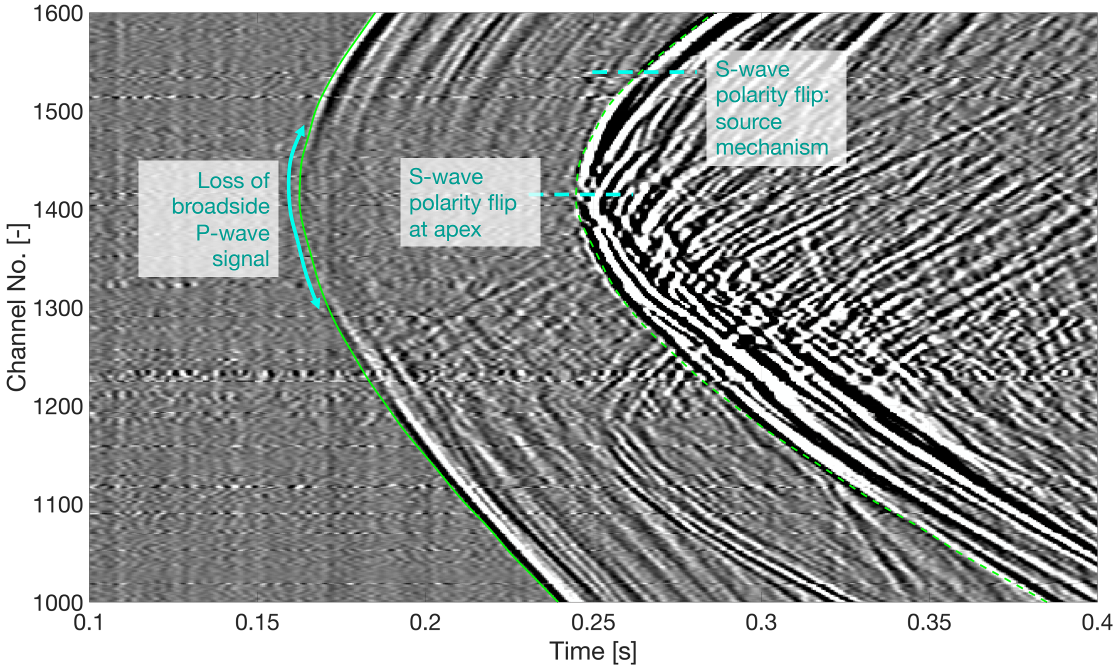

Figure 6: Close-up view of the apexes of the P- and S-wave hyperbolae for an example event. There is a loss of broadside P-wave energy at the apex. The S-wave component experiences a polarity flip at the apex, which is used to pick the zero-offset channel, and the S-wave arrival time at the apex. The loss of P-wave energy means that the P-wave arrival time at the apex cannot be picked directly. Nevertheless, this pick can be made and adjusted such that the modeled P- (solid green line) and S-wave (dashed green line) arrival times match the observed data. Note that a second polarity flip is also observed in the S-wave arrival at channel 1530 – this is likely to be a source mechanism effect.

Figure 7 shows a synthetic S-wave arrival generated using the SAVA (Köhn et al., 2015) finite-difference code (see Baird et al. (2019) for full model details). The wavefield is sampled at regularly-spaced intervals along a modelled cable. Figure 7a shows the particle velocity vectors for a horizontally polarised S-wave – the particle velocity is parallel to the cable axis. Figure 7b shows the resulting particle motion velocities parallel to the cable axis – velocity is maximised at the broadside channel. However, Figure 7c shows the resulting strain-rate, which is what the DAS array records. At the broadside channel, this is a stationary point, i.e., 0. The polarity of the strain-rate is flipped across the broadside point. This phenomenon therefore provides a simple way of identifying the apex or broadside channel, as the reversal in S-wave polarity is usually fairly easy to observe and manually pick, as shown in Figure 6.

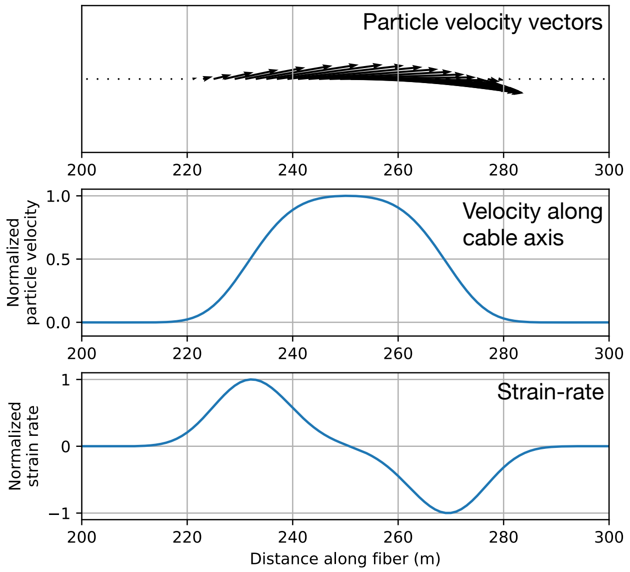

Figure 7: Modeled particle velocities from a broadside S_H-wave arrival. The particle velocity is maximised at the broadside point. However, the DAS array records strain rate, the spatial derivative of particle velocity – this is zero at the broadside point, with a polarity flip on either side.

Having picked the zero-offset channel, and the S-wave arrival time at this channel, we return to consider the zero-offset P-wave arrival time which, as described above, cannot be directly observed as the DAS array cannot record broadside P-wave energy. However, this parameter defines the distance of the event from the array, which affects the moveout of both the P-wave and S-wave arrivals across the entire array. Therefore, rather than attempting to make a P-wave pick on the broadside trace, where the P-wave arrival is not visible, we select and adjust a P-wave arrival time such that the modeled arrival time curves for both P and S phases match the moveout across the array in the observed data (e.g., Figure 6).

The final parameter that must be defined is θ, the polar angle of the cylindrical coordinate system defined in Figure 5. The effect of θ on the arrival times is demonstrated in Figure 8: the principal impact is on the vertical portion of the array, since the position of the event above, below or to the side of the array will have a significant impact on the distance to the vertical portion of the well. Therefore, we are able to adjust θ until a match between the modeled and observed arrival times is obtained. This match is assessed manually, rather than with any qualitative criteria, since qualitative criteria would require automatic picks that, as described above, we wish to avoid for a rapid, manual event location workflow.

Evidently, this requires that the signal is recorded on the vertical part of the array, which in our case study is achieved by the combination of interrogator and engineered fiber-optic cable, as opposed to standard telecommunications cables, providing improved sensitivity across the array (see Case Study description). The use of this method will therefore be limited by the size of event from which arrivals on the vertical part of the array will be visible above the noise levels. For this dataset, we do not have a response function to convert amplitudes recorded by the DAS array from instrument units into a physical unit from which magnitudes could be determined, and so we are not able to comment directly on the distance-magnitude relationships over which such signals could be identified. Nevertheless, we note that for this dataset, almost all of the detected events had signal that could be observed on the vertical part of the array, which in this case is approximately 1000 m from the active stage. Taking a wider view, the detectability of signals on the vertical part of the array will be strongly dependent on the velocity and attenuation structure at a given site, and on the background noise conditions.

Similarly, the approach outlined here relies on a velocity model that is accurate over quite a wide spatial extent, since travel times must be simulated from potential event locations to every receiver channel. Here, we assumed and 1D block model, and found that it performed reasonably well, as demonstrated by the fit between modeled and observed travel times (e.g., Figures 6 and 8). However, as the volume of rock considered grows larger, the ability of a 1D model to represent it grows smaller, and 3D models may be required. Again, the extent to which this is the case will vary on a site by site basis.

Finally, we note that in Figure 8, θ has a small but noticeable effect on the moveout curves within the horizontal part of the array as well. This is because the position of the event above or below the array will determine the layer(s) within the 1D layered velocity model that the arrivals travel through. Therefore, some degree of iteration may be required to search for the combination of P-wave arrival time pick and the θ angle that produces the best fit to the observed wavefield moveout. In this case we anticipate that events will primarily occur near to the injection depths, and so the need for iteration can be minimised by making an appropriate assumption for the θ angle when making the initial P wave pick, although this step is not a necessary condition, as evidenced by our location of some events (Cluster 3, see below) a significant distance above the injection well.

Moreover, the dependence of the wavefield moveout on the θ angle raises the possibility that the angular ambiguity may be resolvable even in cases where signals are not recorded on the vertical part of the array (Baird et al., 2019). This would clearly require a detailed and well-constrained knowledge of the anisotropic velocity model above and below the array, since this effect is relatively small.

The remaining location ambiguity, once the three parameters described above have been constrained, is one of mirror symmetry across the plane defined by the well trajectory. Events in equivalent positions on either side of this plane will produce identical arrival times, and therefore they cannot be discriminated. Here we resolve this ambiguity by placing all events on the southern side of the array, in the direction of the hydraulic fracture treatment well. This ambiguity is no different to the 180° ambiguity produced by a single 1D geophone array where the particle motion is used to define the event azimuth from the well. For geophone arrays, Jones et al. (2010) demonstrated a way of resolving this using the particle motion dip, although in many cases this issue is resolved by, as we do here, placing the events on the side of the array towards the treatment zone. While the 3C particle motion recorded by geophones always provides this option of using the Jones et al. (2010) method, for DAS arrays this ambiguity could only be resolved if recordings were made in multiple monitoring wells simultaneously (e.g., Williams et al., 2017).

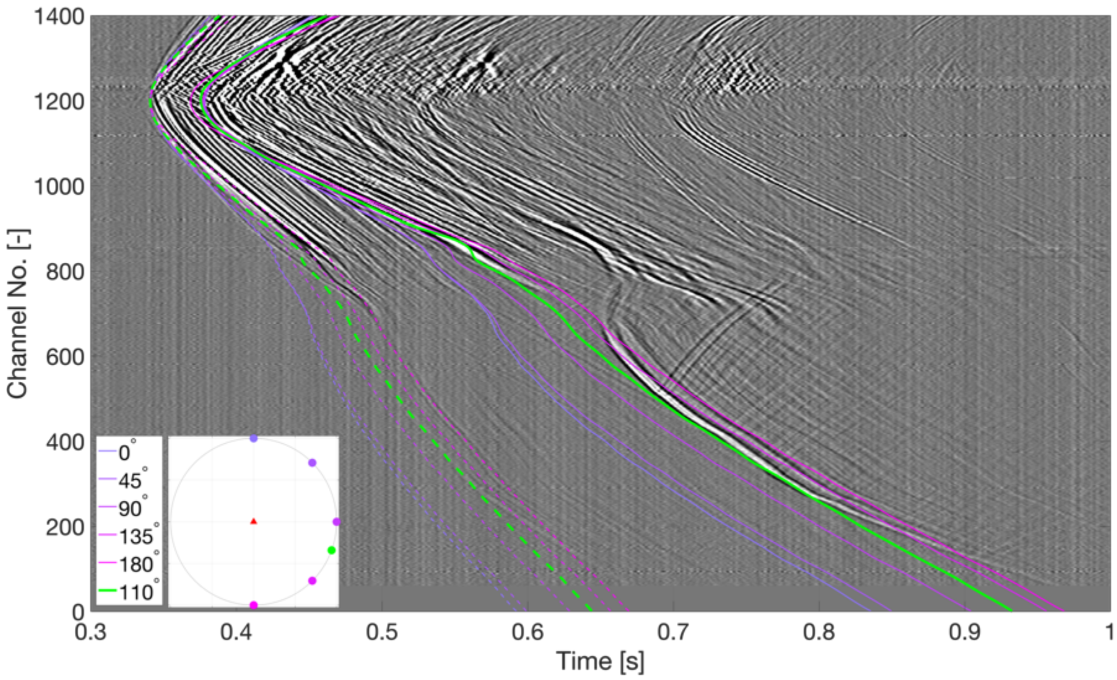

Figure 8: Example event showing how the angle θ of the event from the array impacts the P-wave (dashed lines) and S-wave (solid lines) arrival times. The purple-shaded lines show modeled arrivals for $0 < \theta < 180^o$ in 45^o increments, shown by the coloured dots around the well (viewed along its horizontal axis) in the inset panel, as well as the preferred angle of $\theta = 110^o$ for this event. The primary effect of θ is on the arrivals on the vertical part of the array (channels 1 – 650). However, we note that θ also has a smaller effect on the moveout within the horizontal part of the well – this is because events from above, below and to the side of the well may travel through rocks with different velocities (see Figure 3).

RESULTS

We perform the manual location procedure described above for all 342 detected events. Figure 9 shows the resulting locations. Events are clustered around the perforation interval, as might be expected during hydraulic fracturing, extending to either side of the well perpendicular to its trajectory (parallel to the *y* axis). In depth, the events are found at the depth of the well and extending down to 100 m below. We do not have any data regarding the geomechanical conditions at this site, or of the hydraulic fracturing treatment parameters. Nevertheless, these observations match what might typically be expected from a normal hydraulic fracture, with event locations originating at the perforations and tracking the propagation of hydraulic fractures away from the well.

In more detail, we subdivide the events into three clusters (Figure 9): C1 contains the largest number of events. It is sited at the further end of the perforation interval, and extends parallel to the *y* axis roughly 300 m north and 170 m south of the well. Most of the earlier events during stimulation are found in this cluster. The second cluster, C2, is found at the nearer end of the perforation interval, again extending parallel to the *y* axis. There is a distinct shift in the focus of microseismicity from C1 to C2 during the stimulation period. We interpret these clusters as representing the growth of multiple hydraulic fractures from the well. Finally, six events are observed to occur in a separate cluster, again trending parallel to the *y* axis, roughly 300 m further along, to the south of, and 400 m shallower than the treatment well. Our interpretation is that this corresponds to a pre-existing feature that is perhaps being reactivated by poro-elastic stress transfer produced by the hydraulic fracturing (e.g., Deng et al., 2016). We note that in the surface microseismic data, which covers multiple stages within the well, this C3 feature experiences microseismicity during many of the stages. The purpose of this paper is not to provide a detailed interpretation of the microseismicity – nevertheless these observations serve to show the quality of observation that can be provided by a DAS array used for microseismic monitoring, providing sufficient numbers of events detected, and sufficient precision of event location, to characterise hydraulic fractures in detail.

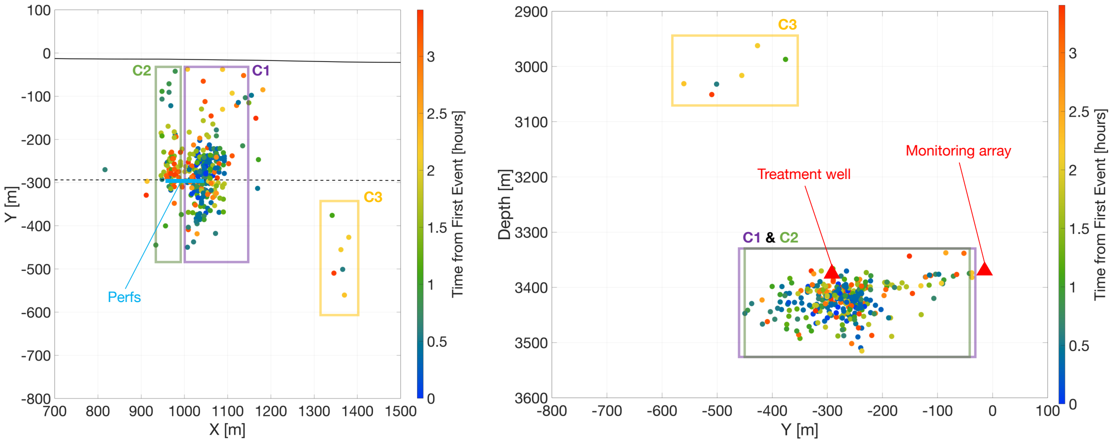

(a) *(b)*

Figure 9: Map view (a) and cross-section (b) of the event locations as provided by the manual picking approach. Events are colored by occurrence time, the monitoring well is shown with a solid black line, the hydraulic fracturing well by the dashed line, and the perforation interval is shown by the light blue line. Events are grouped into three clusters as indicated.

DISCUSSION

Comparison with Surface Microseismic Events

Surface-based microseismic monitoring was also acquired at this site, and this provides an opportunity to compare the performance of the different array types. During the period of study, the surface array detected and located 49 events. We use the event origin times to co-identify events detected by each array, where we assume that an event is co-identified by both the surface and DAS arrays if it has origin times within a window of 1.0 s are found in both catalogues. In some cases, multiple DAS events are observed within a very short time window (see the section on Multiple Repeating Events). In such cases, we select the event with the largest amplitudes on the DAS array as being that which was most likely to be observed by the surface array.

Of the 49 events detected at the surface, 43 were also identified by the DAS array using the method described above, a detection rate of 88 %. In comparison, of the 342 events detected by the DAS array, only 43 were detected by the surface array, a 13 % detection rate. Clearly, the DAS array provides a marked improvement in event detection – this is not surprising since the DAS array is considerably closer to the source region, and so signal strength will be higher.

Figure 10 compares the locations of the DAS array and surface-recorded microseismic events. In a broad sense, both arrays produce similar results – the more distant cluster C3 is seen in both cases, while the remainder of the events are found near to the well perforation. However, the event cloud produced by the surface array is considerably more diffuse than the DAS array locations, with the majority of events being placed to the south of the well, and up to 500 m away. In contrast, the DAS array locations are more tightly clustered, and spread more evenly to the north and south of the treatment well. The precision of event location is such that two clear sub-clusters (C1 and C2 in Figure 9) can be identified, which is not possible for the more diffuse event cloud produced by the surface array. In depth view, the surface microseismic events are scattered over more than 200 m above and below the treatment well, whereas the DAS array events are all found at the depth of the well, or to within 100 m below it. The increased uncertainty in depth for surface vs downhole arrays in particular is a well-acknowledged issue (e.g., Eisner et al., 2009).

The C3 events are found to be systematically 200 m shallower by the DAS array in comparison to the surface microseismic. Without an independent way of ground-truthing, it is not possible to ascertain which of these locations is more accurate.

Overall, the tight clustering of the DAS array locations around the injection interval speaks to the improved precision of these locations in comparison to the surface microseismic, where event locations are much more scattered. The increased precision allows improved interpretation of the observed microseismicity, for example in identifying the two sub-clusters around the perforations, which we have interpreted as representing multiple hydraulic fractures extending from the perforations.

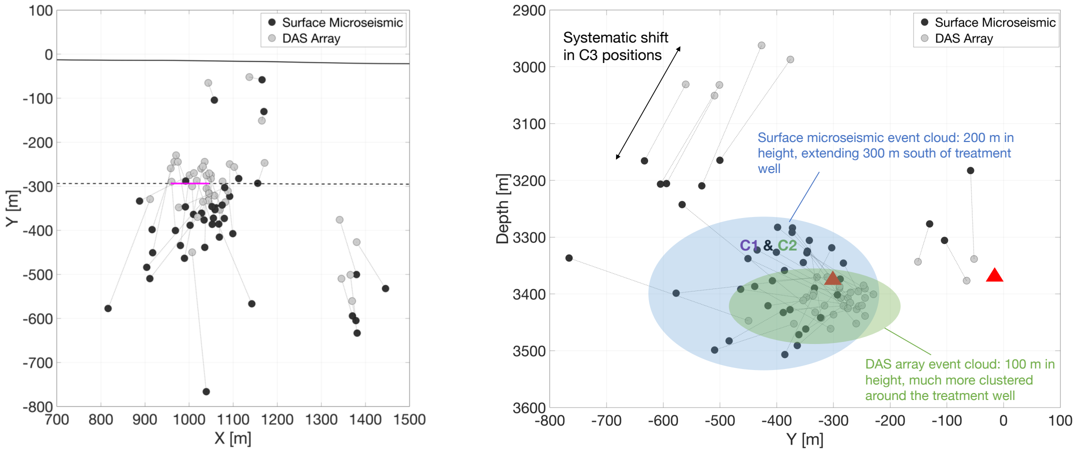

(a) *(b)*

Figure 10: Map view (a) and cross-section (b) comparing event locations from the DAS array (light grey) and surface microseismic array (black). Dashed lines link the

same event located by each array. The two wells are shown by the solid and dashed black lines, while the perforation interval is marked in pink.

Multiple Repeating Events

Figure 11a shows an example microseismic event detected using the detection method outlined above. Closer inspection of these waveforms shows that in fact this "event" consists of four repeating events all occurring within approximately 0.6 s. Repeating events of this nature were common within the dataset studied here, and could be identified by visual inspection of the wavefield images, where the P- and S-wave moveout curves characteristic of an event could be seen easily. Figure 11b shows the same data, but decimated to a single trace per 20 m of array, approximating what might be recorded for the same sequence of events by a geophone array. Because the P- and S-wave arrivals from the multiple events overlap, it becomes difficult to separate and identify them in the geophone data.

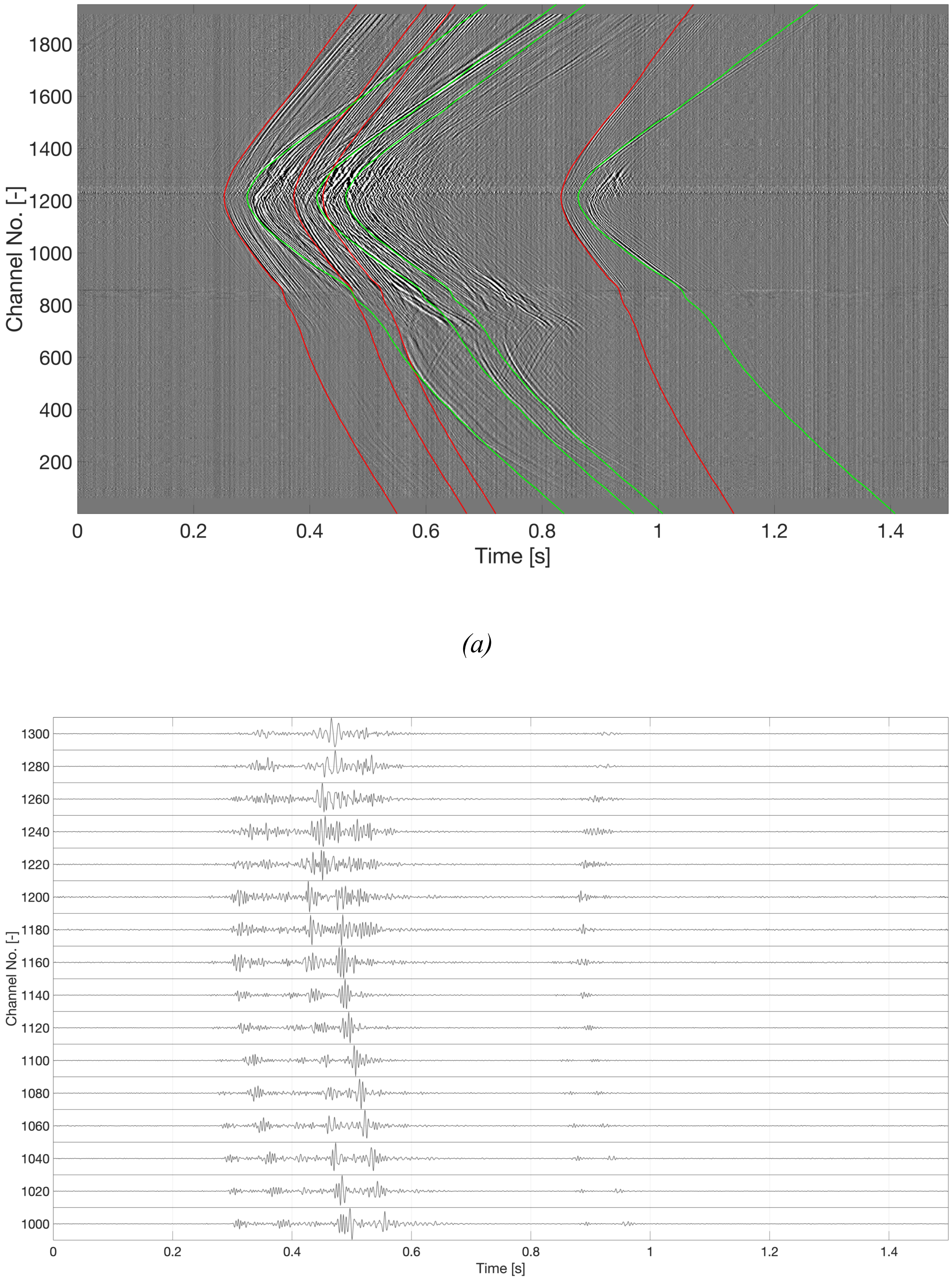

(a)

(b)

Figure 11: Example of multiple events occurring within a short time window – in this case four events occur within approximately 0.6 s. Each P- (red lines) and S-wave (green lines) arrival is marked. The separate events are relatively easy to identify in

the DAS array data (a) through their characteristic moveout curves. In (b) we show the equivalent data as it would appear on a geophone array, with 16 stations spaced every 20 m. Because the P- and S-wave phases from different events overlap, it becomes challenging to identify the different events.

Reservoir Imaging and Subsurface Scatterers

Dyer et al. (2008) showed that pre-existing structures within a reservoir can scatter microseismic energy. These scatterers can be identified by migration-type algorithms applied to the coda of microseismic waveforms. Both Dyer et al. (2008) and Reshetnikov et al. (2015) have applied such methods to the microseismic data recorded using geophone arrays at the Basel geothermal project, finding structures, presumed to be fault zones, that scatter the seismic energy. Similarly, Grechka et al. (2017) applied a migration approach to image hydraulic fractures causing scattering of seismic energy in the Bakken Shale formation.

The advantage of this type of approach is that it enables the detection of structures within the reservoir not identified directly by microseismic event locations. Lin and Zhang (2016) demonstrate this concept using synthetic data and show that, as might be expected, the quality of the migration image will improve substantially as both the aperture of the array and the data fold increase. The above studies were all based on geophone arrays, which have limited aperture and fold. Therefore, identification of scattering in DAS array data, where both the fold and the aperture are significantly larger, could provide a significant improvement in our ability to image reservoir structures.

The high spatial sampling of the microseismic wavefield provided by makes it relatively easy to identify scattered phases. Figure 12 shows an example of such. A coherent arrival is observed (green line in Figure 12a), trailing the P-wave arrival by approximately 0.01 s at its apex, which is positioned off-centre relative to the event itself. The moveout gradient of this arrival is steeper (i.e. indicating a slower velocity) than the P-wave curves, indicating that it may be an S wave. We model the arrival time for a phase that travels as a P wave from the event hypocentre to a scattering point that is centred on the perforation interval, at a distance of 225 m to the north of the well, before being scattered as an S wave to be recorded along the array (as shown in Figure 12b). We find that this modeled arrival time (green line in Figure 12a) produces a very close match to the observed scattering. The position of this scattering point is consistent with where one might expect the tips of the hydraulic fractures to be positioned, and our inference is that the observed arrival represents the scattering of the microseismic waveform as it interacts with a hydraulic fracture.

It is beyond the scope of this paper to perform a full migration imaging study on this dataset (as performed by Grechka et al., 2017, for example), and we note that imaging of this kind will suffer from the same inherent angular ambiguity as event locations unless the scattered energy can be recorded on both the vertical and horizontal parts of the fiber, or if more than one fiber is used to acquire data from adjacent wells. Nevertheless, we note that the large aperture and data fold provided by DAS array data offers significant potential for improved microseismic imaging compared to downhole geophone arrays, and that the high spatial sampling of the wavefield allows scattered phases to be identified relatively easily. Therefore the possibilities identified here merit further investigation.

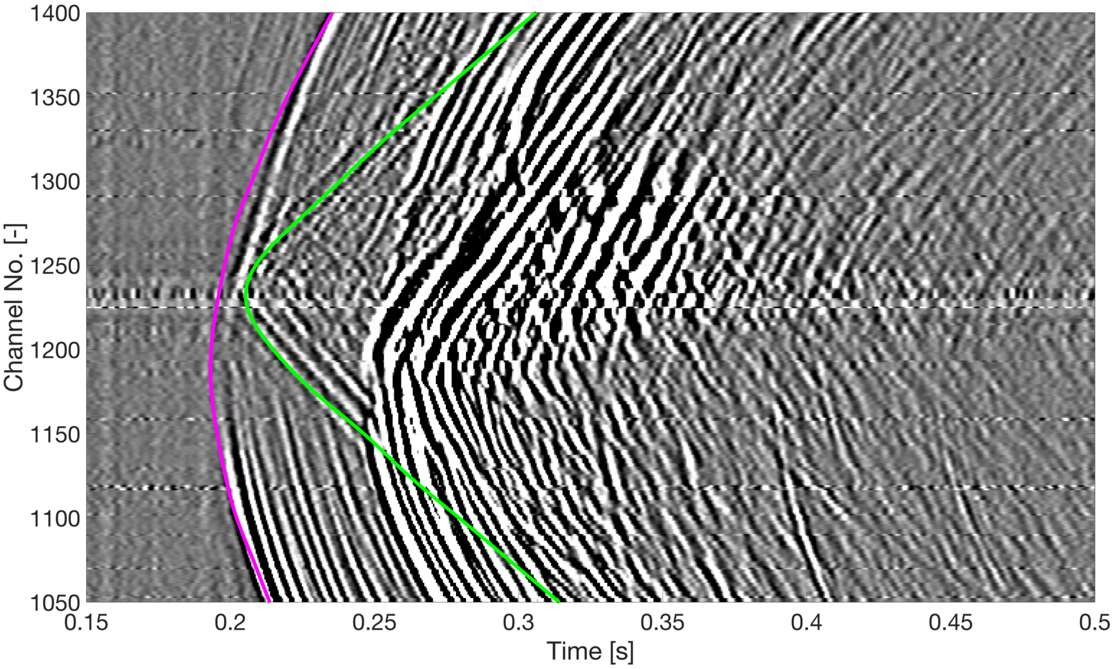

(a)

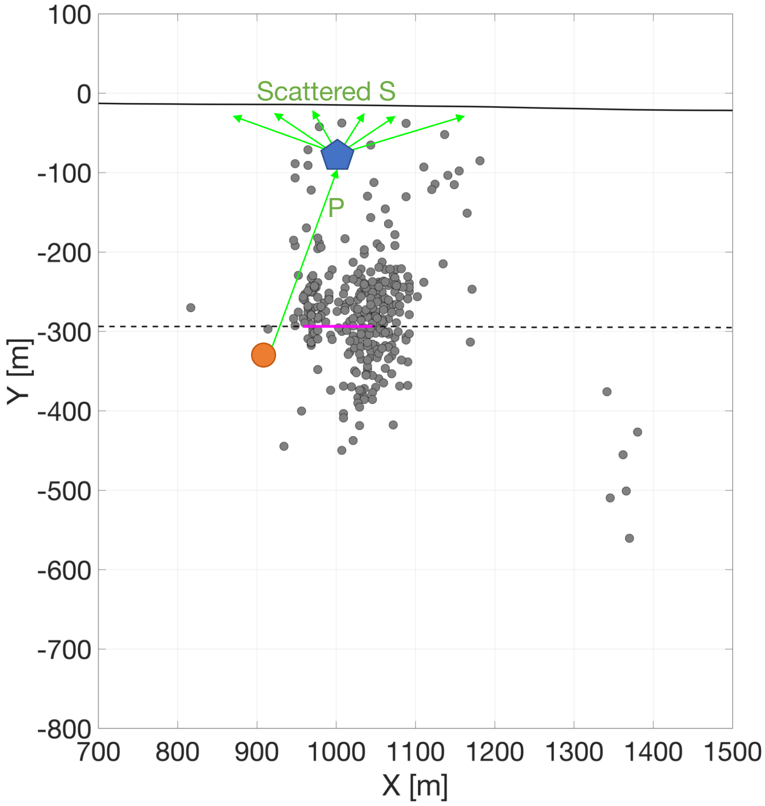

(b)

Figure 12: Example of scattering observed within a microseismic waveform. In (a) we show the recorded data from the event shown by the orange circle in map view in (b). The pink curve in (a) shows the modeled P-wave arrival, while the green curve shows the modeled arrival for a P- to S-wave conversion being scattered from the point marked by the blue pentagon on (b). In (a) we observe an arrival that initiates at channel 1,240 and follows the modeled P-to-S conversion travel-time very closely. Solid and dashed lines in (b) show the monitoring and treatment wells, respectively.

Conclusions

We present a case study demonstrating the use of DAS array data to detect and locate microseismic events during hydraulic fracturing. We use a relatively simple algorithm to detect events, which nevertheless takes advantage of the high fold provided by DAS array data, enabling us to detect a large number of events (on average an event per 35 s) with a minimal rate of false positive detection. While more involved approaches to event detection are being developed, this shows that simple, computationally inexpensive methods can be successful.

We develop a manual procedure to locate events. Locations are defined within a cylindrical coordinate system along the horizontal axis of the array. The location is determined by picking the broadside (or zero-offset) channel, which can be identified by a characteristic S-wave polarity reversal, and the apexes of the P- and S-wave arrivals, such that the modelled moveout matches that observed in the data. The angle θ of the event from the array is constrained from the arrival times on the vertical part of the array. The use of an engineered fibre and improved interrogator provides a substantial improvement in signal strength such that this is possible.

The resulting event locations are found to be closely constrained around the perforation interval, with the exception of a more distant cluster of events, which may represent re-activation of a pre-existing structure via poroelastic effects. Within the event cloud, location precision is such that features can be resolved within it, which we interpret as the propagation of multiple hydraulic fractures.

We compare the DAS array locations to those provided by a surface microseismic array. The DAS array is able to detect many more events than the surface array. Moreover, the DAS array locations are much more tightly clustered around the perforations, whereas the surface-based event locations are much more scattered, such that it is difficult to identify details within the event cloud. While an independent ground-truth is not possible, it seems apparent that the DAS array locations have much greater precision than those provided by the surface array.

Finally, we explore some features of further interest within the DAS data. We note that many events appear to occur as repeating events tightly clustered in time, with multiple events per second. Because the different phases generated by such sequences will overlap in time, identifying this with geophone data may be more challenging. However, the distinctive shapes of the P- and S-wave moveout curves on a DAS array allow them to be identified. While we do not attempt further interpretation here, this observation of multiple repeating events may have significance for understanding hydraulic fracture propagation and microseismic event nucleation.

The wide aperture and high fold of DAS data should be ideally suited for using microseismic waveforms to image reservoirs using migration-based techniques to image scattering points (such as faults or existing hydraulic fractures). Although we do not perform a migration analysis in this study, we note that in our data we are able to observe scattered phases that are consistent with P-wave to S-wave conversions from the tips of the hydraulic fractures. However, scattered phases would need to be observed on both the vertical and horizontal parts of the well, or on multiple adjacent arrays, for locations of scattering points to be fully constrained.

We anticipate that the various advantages described above, plus some of the logistical benefits of using DAS arrays, will mean that this method will become increasingly common for microseismic monitoring. If so, we anticipate that observations such as these will become increasingly important for imaging subsurface reservoirs.

References

Allen R.V., 1978. Automatic earthquake recognition and timing from single traces: Bulletin of the Seismological Society of America 68, 1521-1532.

Baird A., A. Stork, S. Horne, G. Naldrett, M. Kendall, J. Wookey, A. Clarke, and J. Verdon, 2019. Modelling of fibre-optic DAS response to microseismic arrivals in anisotropic media: EAGE Annual Conference, Expanded Abstracts We_R09_08, London.

Binder G. and D. Chakraborty, 2019. Detecting microseismic events in downhole distributed acoustic sensing data using convolutional neural networks: SEG Annual Conference, Expanded Abstracts, 4864-4868.

Chambers K., Kendall J-M., Brandsberg-Dahl S., and J. Rueda, 2010. Testing the ability of surface arrays to monitor microseismic activity: Geophysical Prospecting 58, 821-830.

Clarke H., J.P. Verdon, T. Kettlety, A.F. Baird, and J-M. Kendall, 2019. Real time imaging, forecasting and management of human-induced seismicity at Preston New Road, Lancashire, England: Seismological Research Letters 90, 1902-1915.

Daley T.M., D.E. Miller, K. Dodds, P. Cook, B.M. and Freifeld, 2016. Field testing of modular borehole monitoring with simultaneous distributed acoustic sensing and geophone vertical seismic profiles at Citronelle, Alabama: Geophysical Prospecting 64, 1318-1334.

Deng K., Y. Liu, and R.M. Harrington, 2016. Poroelastic stress triggering of the December 2013 Crooked Lake, Alberta, induced seismicity sequence: Geophysical Research Letters 43, 8482-8491.

Duncan P.M. and L. Eisner, 2010. Reservoir characterization using surface microseismic monitoring: Geophysics 75, A139-A146.

Dyer B.C., U. Schanz, F. Ladner, M.O. Häring, and T. Spillman, 2008, Microseismic imaging of a geothermal reservoir stimulation: The Leading Edge, 27, 856–869.

Eisner L., P.M. Duncan, W.M. Heigl, and W.R. Keller, 2009. Uncertainties in passive seismic monitoring: The Leading Edge 28, 648-655.

Grechka V., Z. Li, B. Howell, H. Garcia, and T. Wooltorton, 2017. High-resolution microseismic imaging: The Leading Edge 36, 822-828.

Jones G.A., D. Raymer, K. Chambers, and J-M. Kendall, 2010. Improved microseismic event location by inclusion of a priori dip particle motion: a case study from Ekofisk: Geophysical Prospecting 58, 727-737.

Karrenbach M., D. Kahn, S. Cole, A. Ridge, K. Boone, J. Rich, K. Silver, and D. Langton, 2017. Hydraulic-fracturing-induced strain and microseismic using in situ distributed fiber-optic sensing: The Leading Edge 36, 837-844.

Karrenbach M., S. Cole, A. Ridge, K. Boone, D. Kahn, J. Rich, K. Silver, and D. Langton, 2019. Fiber-optic distributed acoustic sensing of microseismicity, strain and temperature during hydraulic fracturing: Geophysics 84(1), D11-D23.

Köhn D., O. Hellwig, D. De Nil, and W. Rabbel, 2015. Waveform inversion in triclinic anisotropic media - a resolution study: Geophysical Journal International 201, 1642-1656.

Kurzon I., F.L. Vernon, A. Rosenberger, and Y. Ben-Zion, 2014. Real-time automatic detectors of P and S Waves using singular value decomposition: Bulletin of the Seismological Society of America 104, 1696-1708.

Lin Y. and H. Zhang, 2016. Imaging hydraulic fractures by microseismic migration for downhole monitoring system: Physics of the Earth and Planetary Interiors 261, 88-97.

Lomax A., C. Satriano, and M. Vassallo, 2012. Automatic picker developments and optimization: FilterPicker – a robust, broadband picker for real-time seismic monitoring and earthquake early warning: Seismological Research Letters 83, 531-540.

Mateeva A., J. Lopez, H. Potters, J. Mestayer, B. Cox, D. Kiyashchenko, P. Wills, S. Grandi, K. Hornman, B. Kuvshinov, W. Berlang, Z. Yang, and R. Detomo, 2014. Distributed acoustic sensing for reservoir monitoring with vertical seismic profiling: Geophysical Prospecting 62, 679-692.

Maxwell S.C., J. Rutledge, R. Jones, and M. Fehler, 2010. Petroleum reservoir characterization using downhole microseismic monitoring: Geophysics 75(5), A129-A137.

Molteni D., M.J. Williams, and C. Wilson, 2017. Detecting microseismicity using distributed vibration: First Break 35, 51-55.

Mondanos M. and T. Coleman, 2019. Application of distributed fibre-optic sensing to geothermal reservoir characterization and monitoring: First Break 37, 51-56.

Oye V. and M. Roth, 2003. Automated seismic event location for hydrocarbon reservoirs: Computers and Geosciences 29, 851-863.

Parker T., S. Shatalin, and M. Farhadiroushan, 2014. Distributed acoustic sensing – a new tool for seismic applications: First Break 32, 61-69.

Reshetnikov A., J. Kummerow, H. Asanuma, M. Häring, and S.A. Shapiro, 2015. Microseismic reflection imaging and its application to the Basel geothermal reservoir: Geophysics 80, WC39–WC49.

Richter P., T. Parker, C. Woerpel, Y. Wu, R. Rufino, and M. Farhadiroushan, 2019. Hydraulic fracture monitoring and optimization in unconventional completions using a high-resolution engineered fibre-optic Distributed Acoustic Sensor: First Break 37, 63-68.

Sethian J. and A. Popovici, 1999. 3-D traveltime computation using the fast marching method. Geophysics 64, 516-523.

Sleeman R. and T. van Eck, 1999. Robust automatic P-phase picking: an on-line implementation in the analysis of broadband seismogram recordings: Physics of the Earth and Planetary Interiors 113, 265-275.

Tselentis G-A., N. Martakis, P. Paraskevopoulos, A. Lois, and E. Sokos, 2012. Strategy for automated analysis of passive microseismic data based on S-transform, Otsu's thresholding, and higher order statistics: Geophysics 77(6), KS43-KS54.

Webster P., M. Molenaar, C. Perkins, 2016. DAS Microseismic: CSEG Recorder 41, 38-39.

Williams A., J-M. Kendall, A. Clarke, and J.P. Verdon, 2017. Challenges in locating microseismic events using distributed acoustic sensors: AGU Fall Meeting, New Orleans, Abstract S33B-2387.